



# Resolution of chemical shift anisotropy in $^{19}\text{F}$ ENDOR spectroscopy at 263 GHz/9.4 T



Annemarie Kehl<sup>a</sup>, Markus Hiller<sup>a</sup>, Fabian Hecker<sup>a</sup>, Igor Tkach<sup>a</sup>, Sebastian Dechert<sup>b</sup>, Marina Bennati<sup>a,b,\*</sup>, Andreas Meyer<sup>a,\*</sup>

<sup>a</sup>Research Group EPR Spectroscopy, Max Planck Institute for Biophysical Chemistry, Am Fassberg 11, 37077 Göttingen, Germany

<sup>b</sup>Department of Chemistry, Georg August University of Göttingen, Tammannstr. 4, Göttingen, Germany

## ARTICLE INFO

### Article history:

Received 3 September 2021

Revised 14 October 2021

Accepted 15 October 2021

Available online 18 October 2021

### Keywords:

Electron Nuclear Double Resonance

Chemical Shifts

High-Field EPR

Spectral Simulation

Distance Measurements

## ABSTRACT

Pulsed  $^{19}\text{F}$  ENDOR spectroscopy provides a selective method for measuring angstrom to nanometer distances in structural biology. Here, the performance of  $^{19}\text{F}$  ENDOR at fields of 3.4 T and 9.4 T is compared using model compounds containing one to three  $^{19}\text{F}$  atoms.  $\text{CF}_3$  groups are included in two compounds, for which the possible occurrence of uniaxial rotation might affect the distance distribution. At 9.4 T, pronounced asymmetric features are observed in many of the presented  $^{19}\text{F}$  ENDOR spectra. Data analysis by spectral simulations shows that these features arise from the chemical shift anisotropy (CSA) of the  $^{19}\text{F}$  nuclei. This asymmetry is also observed at 3.4 T, albeit to a much smaller extent, confirming the physical origin of the effect. The CSA parameters are well consistent with DFT predicted values and can be extracted from simulation of the experimental data in favourable cases, thereby providing additional information about the geometrical and electronic structure of the spin system. The feasibility of resolving the CSA at 9.4 T provides important information for the interpretation of line broadening in ENDOR spectra also at lower fields, which is relevant for developing methods to extract distance distributions from  $^{19}\text{F}$  ENDOR spectra.

© 2021 The Authors. Published by Elsevier Inc. This is an open access article under the CC BY-NC-ND license (<http://creativecommons.org/licenses/by-nc-nd/4.0/>).

## 1. Introduction

Fluorine has found many applications in medicinal and biophysical chemistry [1], one prominent example being the use of  $^{19}\text{F}$  nuclei as nuclear spin labels for magnetic resonance techniques. For this purpose,  $^{19}\text{F}$  nuclei are attractive owing to their natural scarcity in biology, which enables high selectivity in spectroscopic experiments [2–6]. Furthermore,  $^{19}\text{F}$  labels can often be introduced in proteins without disturbing protein folding or thermodynamic properties [7–10]. Besides,  $^{19}\text{F}$  nuclei have excellent properties for magnetic resonance spectroscopy such as a nuclear spin  $I = 1/2$ , 100% natural abundance, and a high gyromagnetic ratio amounting to 94% of the  $^1\text{H}$  value. The latter enables long-range distance measurements up to 2 nm by NMR, as demonstrated in previous studies using  $^1\text{H}$ - $^{19}\text{F}$  or  $^{19}\text{F}$ - $^{19}\text{F}$  couplings in  $^{19}\text{F}$ -labelled compounds [11–13]. Also a combination of  $^{19}\text{F}$  and paramagnetic nitroxide or lanthanide spin labels has been used to measure distances via paramagnetic relaxation enhancements

or pseudocontact shifts, respectively [14,15]. Finally,  $^{19}\text{F}$  nuclei exhibit a large range of chemical shifts >300 ppm [16] (compared to 15 ppm for  $^1\text{H}$  [17]) which are sensitive to their local environment [18]. This property has been exploited in ligand binding studies or to monitor conformational changes in biomolecules [19–21].

Pulsed electron-nuclear double resonance (ENDOR) spectroscopy is a related technique to detect nuclear spin transitions. It is based on electron paramagnetic resonance (EPR) and relies on the presence of unpaired electron spins. In pulsed ENDOR, the hyperfine coupling (HFC) between a nuclear and an electron spin is probed by monitoring the effect of nuclear spin transitions on the intensity of the electron spin echo [22]. Compared to NMR spectroscopy, ENDOR benefits from the magnetic moment of electron spins largely exceeding that of nuclear spins, resulting in enhanced sensitivity. Furthermore, the applicability of ENDOR in structural biology is not limited by the size of the biomolecules. The combination of  $^{19}\text{F}$  nuclear and electron spins for ENDOR-based distance measurements in biomolecules was pioneered early on by Makinen and co-workers [23,24]. However, strong overlap of  $^1\text{H}$  and  $^{19}\text{F}$  resonances occurs at the low magnetic fields of 0.35 T employed in these studies. This drawback was addressed recently in our laboratory by the application of higher magnetic fields of

\* Corresponding authors.

E-mail addresses: [marina.bennati@mpibpc.mpg.de](mailto:marina.bennati@mpibpc.mpg.de) (M. Bennati), [andreas.meyer@mpibpc.mpg.de](mailto:andreas.meyer@mpibpc.mpg.de) (A. Meyer).

3.4 T, corresponding to an electron spin resonance frequency of 94 GHz (W band). At such fields, the proton and fluorine Larmor frequencies are separated by 8.5 MHz, which prevents overlap of  $^1\text{H}$  and  $^{19}\text{F}$  resonances in most  $^{19}\text{F}$  – nitroxide spin systems. Using the Mims ENDOR sequence [25], it was possible to measure distances up to 15 Å, corresponding to an HFC constant of  $\geq 20$  kHz [26]. Such a small coupling is close to the estimated frequency resolution limit of about 20 kHz imposed by the ENDOR line width [26]. Spin systems with larger  $^1\text{H}$  HFCs than nitroxides will still lead to overlapping resonances though. Prominent examples for such systems would be the internal  $^1\text{H}$  couplings of tyrosyl radicals, for instance in ribonucleotide reductase [27–29] or photosystem II [30–33]. Field strengths of 9.4 T are comparable to typical field strengths in NMR and further increase the separation between the  $^{19}\text{F}$  and  $^1\text{H}$  Larmor frequencies to 24.5 MHz, thereby better preventing overlap of resonances.

Besides this, increasing the polarizing magnetic field leads to further effects on the nuclear hyperfine spectra as demonstrated by us in recent studies. A resolution improvement in  $^1\text{H}$  ENDOR spectroscopy at 9.4 T/263 GHz compared to 3.4 T/94 GHz was achieved and attributed to enhanced orientation selectivity at higher fields, which permitted recognizing conformational distributions [34–36]. In another study we reported 94 and 263 GHz ENDOR spectra of  $^{17}\text{O}$  ( $I = 5/2$ ) quadrupolar nuclei from water bound to radical intermediates in proteins, which showed narrowing of the central  $m_I = \pm 1/2$  nuclear spin transitions with increasing field strengths [37]. Here, we report another effect at this high magnetic field, i.e. the resolution of the chemical shift anisotropy (CSA). The CSA originates from the variations in the local magnetic field due to the distribution of electrons in the molecule [38]. For  $^{19}\text{F}$  nuclei attached to phenyl rings, large anisotropy parameters  $\Delta$  of up to 75 ppm have been reported previously, with principal values of the CSA tensors spanning ranges up to ca. 130 ppm [18]. This would lead to line shifts up to ca. 45 kHz at 9.4 T, which become visible in ENDOR spectra. With that in mind, the common practice of neglecting CSA when analysing ENDOR data requires reconsideration.

In this study,  $^{19}\text{F}$  ENDOR spectroscopy at 263 GHz is explored using five model compounds (**1** – **5**), for which 263 GHz and 94 GHz Mims ENDOR spectra are presented and compared. We show that  $^{19}\text{F}$  ENDOR spectra at 263 GHz become significantly asymmetric. Spectral analysis including the CSA in the spin Hamiltonian is performed using a numerical simulation routine. Analysis of the CSA provides information about the orientation of the fluorinated moieties in a given compound. The selection of compounds enables improved understanding of the resolution limits of ENDOR based distance measurements at both 9.4 and 3.4 T.

## 2. Results and discussion

### 2.1. Preparation and properties of the model compounds

All model compounds relevant for this study are illustrated in Fig. 1. Each compound was synthesized via Steglich esterification in a single step [26]. Compounds **2** – **5** extend the library of  $^{19}\text{F}$  – nitroxide model compounds established in our previous study, where all model compounds were monosubstituted and, despite assuming several conformations, only a single distance was observed in each case. The electron spin echo (ESE) spectra for all compounds are in accordance with previously published data, and for **1** the spectra at both 263 and 94 GHz are shown in Fig. 2 A and B (further details on experiments and simulations of the ESE spectra are given in Figures S1 – S4 of the Supporting Information (SI)). Crystallographic data for all new compounds is presented in the SI. The spectral data, however, is analysed with the support

of DFT optimized structures (xyz-coordinates are given in the SI), which better represent the solution state structure of the compounds [26]. Furthermore, DFT calculations reveal negligible isotropic contributions to the HFC tensor for all compounds (typically  $\leq 5$  kHz). Compound **1** bears a single  $^{19}\text{F}$  atom attached to a rigid phenyl ring in 6.7 Å distance to the centre of the electron spin density. Two conformations **a** and **b** with different populations are expected for **1** (Fig. 1B and D), but only a single Pake pattern was resolved in our previous study at 94 GHz [26]. To avoid overparameterization, only the predominant conformation **1a** will be considered in this work. The new compounds **2** and **3** bear two  $^{19}\text{F}$  nuclei. In **2**, the two expected inter-spin distances amount to 6.7 Å and 9.4 Å, similar to the distances in **1** and **6**. In **3**, the expected difference between the two inter-spin distances is much smaller, and **3** should approximate a superposition of the two conformations **1a** and **1b**. Finally, compounds **4** and **5** bear trifluoromethyl groups. In contrast to the fully rigid  $\text{C}_{\text{Ar}}\text{-F}$  groups, these groups possess a uniaxial rotational degree of freedom (Fig. 1C). If the group rotates freely, a single, dipolar HFC tensor [39–41] as well as a single, axially averaged CSA tensor would be measured [42]. Because the resulting resonance would represent three  $^{19}\text{F}$  nuclei, enhanced sensitivity would be expected, too [43]. If no rotation of the group on the time scale of the ENDOR experiment occurs, observation of three different dipolar HFC tensors along with potentially different CSA contributions would be expected instead. While this might be useful information for structural modelling, the number of parameters might pose an additional challenge during analysis.

### 2.2. Implementing chemical shifts in ENDOR data analysis.

The spin Hamiltonian for a nitroxide radical coupled to a  $^{19}\text{F}$  nucleus consists of two main components. The first part describes the spin system of the nitroxide (i.e. the electron spin with  $S = 1/2$  and the strongly coupled  $^{14}\text{N}$  nucleus with  $I = 1$ ) and the second part describes the spin system of the more distant  $^{19}\text{F}$  nucleus ( $I = 1/2$ ) coupled to the electron spin. These two parts can be written as:

$$\hat{H}_{\text{S}} = \hat{H}_{\text{S,EPR}} + \hat{H}_{\text{S},^{19}\text{F ENDOR}} \quad (1)$$

In the following we will use the notation  $I_1$  for the  $^{14}\text{N}$  and  $I_2$  for the  $^{19}\text{F}$  nuclear subspaces, respectively.  $\hat{H}_{\text{S,EPR}}$  accounts for the electron Zeeman term as well as the nuclear Zeeman, hyperfine and quadrupole coupling terms of  $^{14}\text{N}$ :

$$\begin{aligned} \hat{H}_{\text{S,EPR}} &= \hat{H}_{\text{EZ}} + \hat{H}_{\text{NZ}}(^{14}\text{N}) + \hat{H}_{\text{HFC}}(^{14}\text{N}) + \hat{H}_{\text{NQC}}(^{14}\text{N}) \\ &= \mu_{\text{B}} \mathbf{B}_0 \mathbf{g} \hat{\mathbf{S}} - \mu_{\text{N}} g_{\text{n},1} \mathbf{B}_0 \hat{\mathbf{I}}_1 + h \hat{\mathbf{S}} \mathbf{A}_1 \hat{\mathbf{I}}_1 + h \hat{\mathbf{I}}_1 \mathbf{P}_1 \hat{\mathbf{I}}_1 \end{aligned} \quad (2)$$

where  $\mu_{\text{B}}$  and  $\mu_{\text{N}}$  are the Bohr and nuclear magnetons,  $\mathbf{g}$  is the electronic  $g$  tensor and  $g_{\text{n},1}$  the  $^{14}\text{N}$  isotropic nuclear  $g$  value,  $\mathbf{B}_0$  is the magnetic field vector,  $\hat{\mathbf{S}}$  and  $\hat{\mathbf{I}}_1$  are the electronic and  $^{14}\text{N}$  nuclear spin vector operators, and  $\mathbf{A}_1$  and  $\mathbf{P}_1$  are the  $^{14}\text{N}$  hyperfine and the quadrupole coupling tensors, respectively [44–46]. The Hamiltonian part  $\hat{H}_{\text{S,EPR}}$  can be treated separately from the second part  $\hat{H}_{\text{S},^{19}\text{F ENDOR}}$  by assuming the high field approximation for the electron spin ( $E_{\text{EZ}} \gg E_{\text{HFC},1}$  and small  $g$  anisotropy, i.e.  $g_{\text{max}}/g_{\text{min}} \approx 1$ ) as well as  $E_{\text{HFC},1} \gg E_{\text{NQC},1}$  [47]. The HFC part of  $\hat{H}_{\text{S,EPR}}$  is not diagonal, as it includes the large anisotropic HFC interaction of the  $^{14}\text{N}$  nucleus, which exceeds the  $^{14}\text{N}$  Larmor frequency of  $\sim 29$  MHz at an external field of 9.4 T. Nevertheless, the  $\hat{\mathbf{I}}_1$  subspace can be diagonalized up to pseudo-first order (i.e. neglecting terms of the form

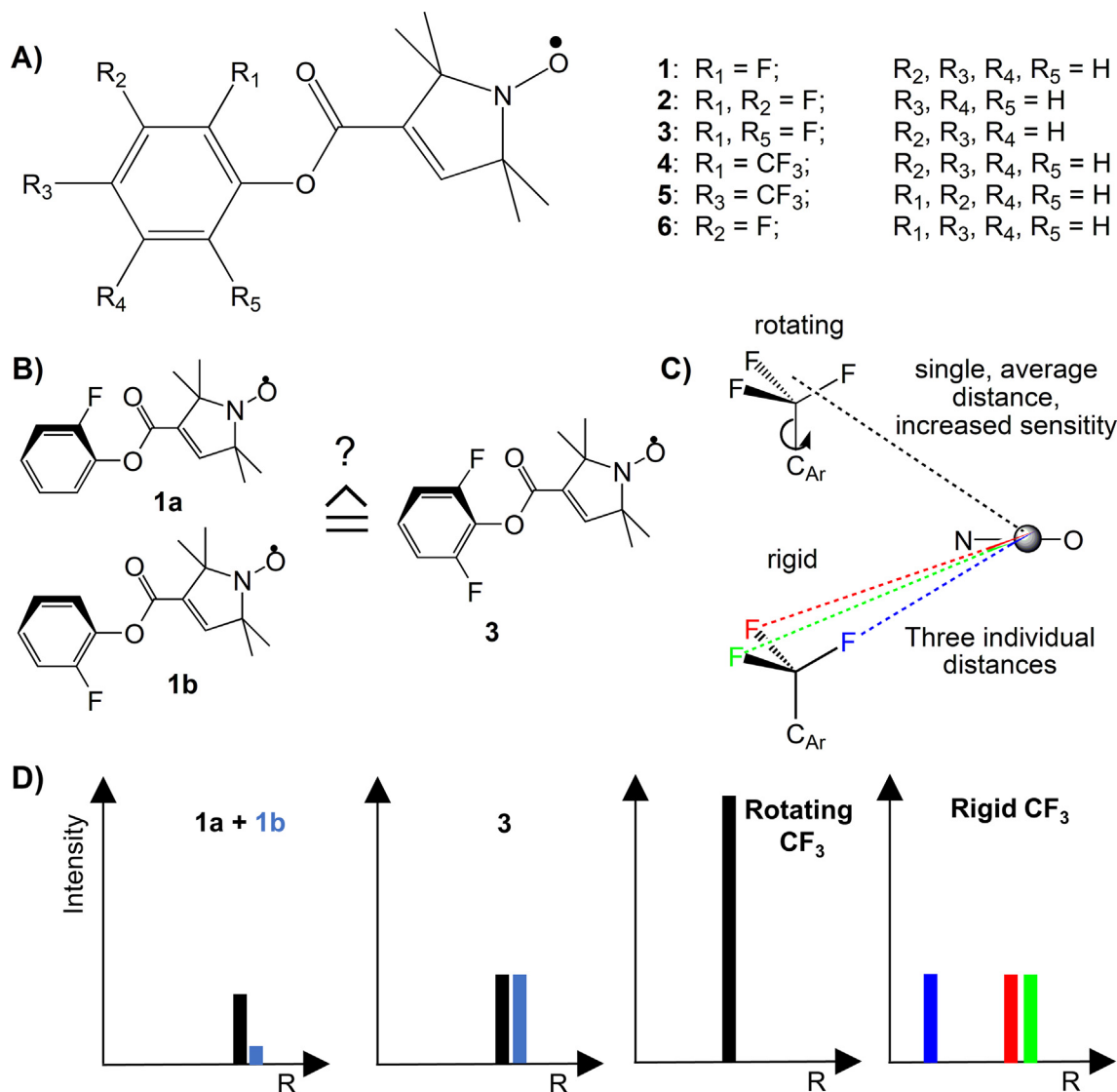


**Fig. 1.** (A) Model compounds investigated in this study. Compounds **1** and **6** have been presented before [26], compound **6** is only included for discussion. (B) Illustration of the conformational flexibility of the phenyl ring of compound **1**. The positions of the  $^{19}\text{F}$  atoms in **3** resemble those of the two conformations of **1**. (C) Schematic illustration of two limiting cases for the dynamics of the  $\text{CF}_3$  group, the grey sphere represents the center of gravity of the nitroxide's spin density. (D) Schematic illustration of expected  $^{19}\text{F}$  - nitroxide distances for the situations depicted in (B) and (C).

$S_x I_{y,1}$  and  $S_y I_{x,1}$ ) independently from the  $\hat{I}_2$  subspace [45,47]. Instead, the  $\hat{I}_2$  subspace  $\hat{H}_{S,^{19}\text{F}}^{\text{ENDOR}}$  can be considered in the high-field approximation ( $E_{\text{NZ},2} \gg E_{\text{HFC},2}$ ) and expressed as:

$$\hat{H}_{S,^{19}\text{F}}^{\text{ENDOR}} = \hat{H}_{\text{NZ}}(^{19}\text{F}) + \hat{H}_{\sigma}(^{19}\text{F}) + \hat{H}_{\text{HFC}}(^{19}\text{F})$$

$$\approx -\mu_{\text{N}} g_{\text{n},2} (1 - \sigma_{zz}) B_0 \hat{I}_{z,2} + h A_{zz,2} \hat{S}_z \hat{I}_{z,2} \quad (3)$$

where  $\sigma_{zz}$  is the relevant element of the shielding tensor in the laboratory frame [38],  $\hat{S}_z$  is the z component of  $\hat{S}$ , and all other elements have been explained for Equation (2). We note that the high field approximation does not generally hold for  $^{19}\text{F}$ , as very large (>100 MHz)  $^{19}\text{F}$  HFCs were reported also for organic radicals [48]. However, it does for the small HFC values ( $\leq 1$  MHz) encountered in the context of distance measurements. Then, the two allowed  $^{19}\text{F}$  ENDOR transition energies ( $\Delta m_{1,2} = \pm 1$ ) can be written as [45]:

$$\Delta E_{\text{ENDOR}} = \left| -\mu_{\text{N}} g_{\text{n},2} B_0 (1 - \sigma_{zz}) \pm \frac{1}{2} h A_{zz,2} \right| \quad (4)$$

Instead of the shielding  $\sigma$ , we introduce the chemical shift  $\delta$  - as defined by IUPAC - for comparison with values from NMR using a reference compound with isotropic shielding,  $\sigma_{\text{ref}}$  [49]:

$$\delta_{zz} = (v - v_{\text{ref}}) / v_{\text{ref}} = (\sigma_{\text{ref}} - \sigma_{zz}) / (1 - \sigma_{\text{ref}}) \quad (5)$$

We note that in Equation (5),  $v = -\mu_{\text{N}} g_{\text{n}} B_0 (1 - \sigma_{zz}) / h$ , and similarly for  $v_{\text{ref}}$  with  $\sigma_{\text{ref}}$ . By combining Equations (4) and (5), the ENDOR resonance frequencies are reformulated as:

$$v_{\text{ENDOR}} = \left| v_{\text{ref}} + v_{\text{ref}} \cdot \delta_{zz} \pm \frac{1}{2} A_{zz,2} \right| \quad (6)$$

$v_{\text{ref}}$  is taken here as the NMR resonance frequency of  $\text{CFCl}_3$ , in accordance with the practice in liquid state NMR spectroscopy. The reference frequency  $v_{\text{ref}}(\text{CFCl}_3)$  is related to the  $^1\text{H}$  resonance frequency of tetramethylsilane ( $v_{1\text{H}}(\text{TMS})$ ) by the factor  $\Xi$  [50,51]:

$$\Xi = \frac{v_{\text{ref}}(\text{CFCl}_3)}{v_{1\text{H}}(\text{TMS})} = \frac{g_{\text{n}}(^{19}\text{F})}{g_{\text{n}}(^1\text{H})} \cdot \frac{(1 - \sigma_{\text{iso}}(\text{CFCl}_3))}{(1 - \sigma_{\text{iso}}(\text{TMS}))} = 0.94094011 \quad (7)$$

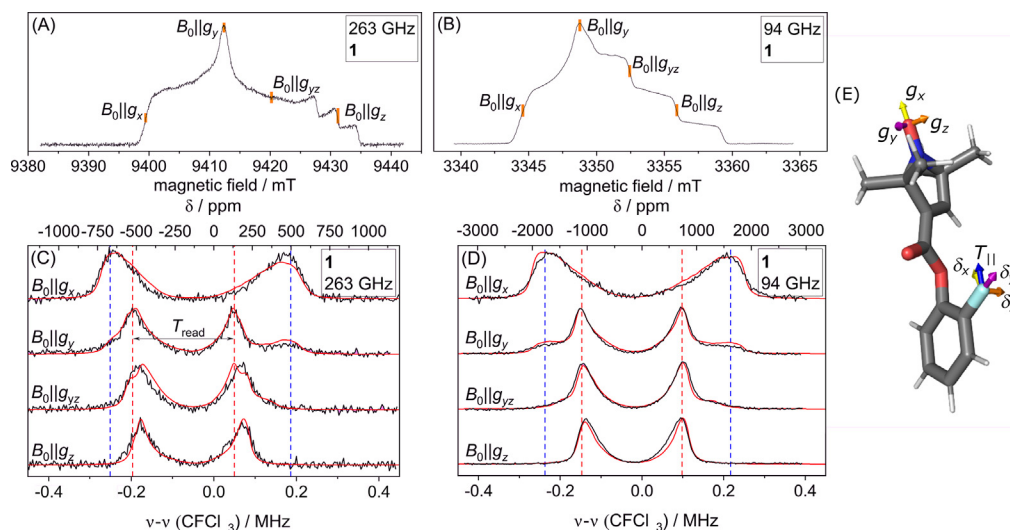


**Fig. 2.** Electron spin echo (ESE) detected spectra of **1** at 263 GHz (A) and 94 GHz (B, data adapted from Ref. [26]) with indication of the excitation for the ENDOR experiments; ENDOR spectra (black) and simulations (red) with parameters listed in Table 1 of compound **1** at 263 GHz (C) and 94 GHz (D, data adapted from Ref. [26]) referenced towards the resonance frequency of  $\text{CFCl}_3$  (see text and Materials and methods) with lines marking the splitting of  $T_{\perp}$  (red) and  $T_{\parallel}$  (blue). All spectra were measured at  $T = 50$  K. (E) Orientation of the simulated  $g$  principal axis frame, the parallel HFC constant ( $T_{\parallel}$ ) and the chemical shift tensor for **1** in the DFT optimized structure.

We note, that  $\Xi = 0.94094011$  in Equation (7) was reported as an experimental observable and its use is recommended by IUPAC [50–52]. Employing this value allows direct comparison of ENDOR derived  $\delta$  values with NMR data. Furthermore and as detailed in Materials and methods, the factor  $\Xi$  is relevant for our experiments, as each orientation-selected ENDOR spectrum is measured at a different external magnetic field value, leading to a variation in the  $^{19}\text{F}$  reference frequency (see Figure S6). A verification of this factor  $\Xi$  is provided in Materials and methods (§ Data processing and  $^{19}\text{F}$  frequency referencing).

For the  $^{19}\text{F}$  HFC tensor  $\mathbf{A}_2$ , the dipolar approximation is used, meaning that the tensor is characterized by a single HFC constant  $T$  and two Euler angles  $\alpha^{\text{HFC}}$  and  $\beta^{\text{HFC}}$ , whereas  $\gamma^{\text{HFC}}$  is set to zero [26]. Equation (8) gives  $\mathbf{A}_2$  in its principal axis system:

$$\mathbf{A}_2 = \mathbf{T} = \begin{pmatrix} T_{\parallel} & & \\ & T_{\perp} & \\ & & T_{\perp} \end{pmatrix} = \begin{pmatrix} 2T & & \\ & -T & \\ & & -T \end{pmatrix} \quad (8)$$

where the subscript ‘2’ for  $^{19}\text{F}$  is omitted from here on for simplicity. The dipolar HFC constant  $T$  depends on the inverse cube of the distance  $R$  between the electron and the nuclear spin (Equation (9)):

$$T = \frac{\mu_0}{4\pi\hbar} \left( \frac{g_e g_n(^{19}\text{F}) \mu_B \mu_N}{R^3} \right) = \frac{C}{R^3} \quad (9)$$

For a  $^{19}\text{F}$  – nitroxide pair ( $g_n(^{19}\text{F}) = 5.257736$ ,  $g_{e,\text{av}} \approx 2.005$ ), the constant  $C$  amounts to 74.52 MHz. As detailed in our previous publication, the use of the dipolar approximation is justified in the case of model compounds like **1** – **5** [26]. We point out that our simulation routine also allows for rhombic hyperfine coupling tensors as well as for inclusion of isotropic coupling constants  $a_{\text{iso}}$ . More details of the simulation procedure are described in Materials and methods.

**Analysis of experimental ENDOR data.** Orientation selective  $^{19}\text{F}$  ENDOR spectra of compound **1** at 9.4 T/263 GHz are shown in Fig. 2C and compared to spectra at 3.4 T/94 GHz in Fig. 2D [26]. The field positions for excitation are marked in the ESE spectra in Fig. 2A and B. Characteristic peaks originating from the perpendicular components of the dipolar Pake pattern are observed in the orientation selective data at both 263 GHz and 94 GHz, which

enables reading-out the dipolar HFC constant  $T$  as indicated in Fig. 2C and an estimation of the inter-spin distance  $R$  using Equation (9) [26]. At 263 GHz, a pronounced asymmetry in the ENDOR spectrum is noted (Fig. 2C), which is much less pronounced at 94 GHz (Fig. 2D). This asymmetry is most pronounced at the field position  $B_0||g_y$ , where the perpendicular component of the dipolar HFC tensor is visible as sharp peaks (red dashes), while the parallel component is visible as two shoulders (blue dashes) with a much smaller extension at the low frequency side than at the high frequency side. The two resolved HFC features originate from different molecular orientations of **1** with respect to  $B_0$ , which implies that their chemical shifts will be different, too. At  $B_0||g_x$  mainly the parallel component of the HFC tensor is visible and at  $B_0||g_y$  and  $B_0||g_z$  the perpendicular component dominates (see Fig. 2C, D). As a consequence, the influence of the CSA is not resolved as clearly as at  $B_0||g_y$  and the spectra resemble those obtained at 94 GHz. However, the referencing of the ENDOR frequencies to the resonance frequency of  $\text{CFCl}_3$  (Equations (5) – (7)) reveals that the HFC components are centred differently at each observer position (Fig. 2C). From the experimental data, differences of up to 40 – 50 kHz ( $\sim 110$  – 135 ppm) in the central frequencies can be estimated in the data shown in Fig. 2C, in good agreement with previously reported CSA values [18]. This effect also occurs at 3.4 T, but is reduced by about 65% as the magnetic field is lower by the same factor (Fig. 2D).

Simulations including the CSA as defined in Equations (5) – (7) are shown as red lines in Fig. 2. Table 1 summarizes all EPR parameters used in the simulations and also includes previous experimental data of relevant compounds. The pronounced asymmetry in the ENDOR spectrum at  $B_0||g_y$  at 263 GHz is well reproduced by implementing the CSA tensor in the simulations and, consistently, appears only to a significantly smaller degree in the simulations at 94 GHz.

The orientations of the CSA and  $g$  tensors are illustrated in the DFT derived structure of **1** (Fig. 2E) by vectors representing their principal values as well as the parallel component of the HFC tensor ( $T_{\parallel}$ ). The direction of the  $T_{\parallel}$  vector matches approximately the direction towards the electron spin density, the vector of  $\delta_y$  is aligned with the C-F bond, the  $\delta_z$  vector is aligned perpendicular to the aromatic plane. Owing to the rigidity of the fluorophenyl group, obtaining the orientation of the CSA tensor implies that

**Table 1**

Simulation parameters for the  $^{19}\text{F}$  ENDOR spectra and comparison with previous ENDOR and NMR data. All simulation parameters agree with our DFT predictions within margins of  $\leq 20$  kHz for the HFC constant  $T$ ,  $< 10^\circ$  for the Euler angles, and  $< 3$  ppm for the CSA principal values. The level of uncertainty for  $T$  depends on the resolution of the ENDOR spectra, i.e. 3 kHz for **1** – **4**, 1 kHz for **5**. An uncertainty for the CSA principal values  $\delta$  of approximately 20 – 30 ppm arises from the experimental determination of the  $^1\text{H}$  resonance. The simulated orientation selected spectra react sensitively on changes in the Euler angles  $\alpha^{\text{HFC}}$ ,  $\beta^{\text{HFC}}$ ,  $\alpha^{\text{CSA}}$ ,  $\beta^{\text{CSA}}$ , and  $\gamma^{\text{CSA}}$  when all other simulation parameters are left unchanged, hence small uncertainties of  $\pm 5^\circ$  are estimated. We note explicitly that the actual errors might be larger, as analyzing the error of a multiparametric model requires evaluation of covariances between all simulation parameters. Values for  $T$  and the line width ( $lw$ ) are given in kHz, values for Euler angles  $\alpha$ ,  $\beta$ , and  $\gamma$  are given in degree ( $^\circ$ ), CSA tensor values  $\delta_i$  are given in ppm, values for  $R$  in Å.

	$T$	$\alpha^{\text{HFC}}$	$\beta^{\text{HFC}}$	$\delta_x$	$\delta_y$	$\delta_z$	$\delta_{\text{iso}}$	$\alpha^{\text{CSA}}$	$\beta^{\text{CSA}}$	$\gamma^{\text{CSA}}$	$lw$	$R^a$
Compound 1												
Sim.	260	-158	-19	-54	-119	-230	-134	65	115	120	20	6.6( $\pm 0.1$ )
ENDOR Ref [26]	260	-162	-19	/	/	/	/	/	/	/	26	6.6
NMR 3-F-Tyr <sup>b</sup> Ref [18,54]	/	/	/	-79	-116	-211	-135	/	/	/	/	/
Compound 2												
Sim. ( <i>o</i> -F)	250	-160	-15	-89	-106	-282	-159	130	80	-80	20	6.7( $\pm 0.1$ )
Sim. ( <i>m</i> -F)	90	-168	-16	-70	-118	-245	-144	-127	80	-60	20	9.4( $\pm 0.2$ )
ENDOR ( <i>m</i> -F, <b>6</b> in Fig. 1) Ref [26]	93	-156	-11	/	/	/	/	/	/	/	19	9.3
NMR 2-F-Tyr Ref [54]	/	/	/	-53	-97	-180	-110	/	/	/	/	/
Compound 3												
Sim. (F)	225	-171	-19	-52	-116	-235	-134	-70	100	115	20	6.9( $\pm 0.1$ )
Sim. (F')	250	-162	20	-47	-115	-233	-131	-115	110	123	20	6.7( $\pm 0.1$ )
Compound 4												
Sim. (F)	130	-177	-24	-4	-93	-169	-89	-50	140	-13	25	8.3( $\pm 0.1$ )
Sim. (F')	240	-168	-15	16	-57	-162	-68	-170	110	80	25	6.8( $\pm 0.1$ )
Sim. (F'')	320	-177	-27	10	-61	-164	-72	-127	55	-15	25	6.2( $\pm 0.1$ )
NMR 4-CF <sub>3</sub> -Phe <sup>c</sup> Ref [42]	/	/	/	/	/	/	-65	/	/	/	/	/
Compound 5												
Sim.	50	-4	-16	/	/	/	-75	/	/	/	27	11.4( $\pm 0.2$ )

<sup>a</sup> Distances were calculated using the corresponding  $T$  value and Equation (9). The uncertainty estimates for the  $R$  values follows from the estimated uncertainties in the  $T$  value. <sup>b</sup> The average of the values reported in the two cited studies is given. The individual values of the CSA tensors differ by  $< 3$  ppm in the two studies. <sup>c</sup> Uniaxial rotation led to partial averaging in the cited study. Therefore, only  $\delta_{\text{iso}}$  is given.

the orientation of the whole group, particularly the plane of the aromatic ring, can be inferred from the spectra. So far, no MAS NMR data for **1** or any of the other fluorinated nitroxides reported herein and in ref. 26 have been reported, which would be most informative for a comparison between ENDOR and NMR derived  $\delta$  values. Such measurements are currently performed with collaborators and will be reported in a follow-up paper. Considering our estimated uncertainty of 30 ppm, the orientation and principal values of the CSA tensors are in good agreement with experimental data of fluorobenzenes and -phenols [18,53,54]. Compared to experimental NMR parameters of 3-F-Tyr [18,54], which resembles the aromatic *o*-fluorophenoxy moiety in **1**, absolute deviations on the order 20 – 25 ppm are obtained for  $\delta_x$  and  $\delta_z$ , respectively. We note that a higher precision of the chemical shift values is achieved by NMR because of its superior intrinsic resolution, whereas the orientation of the CSA tensor is more readily derived using orientation selective ENDOR spectra.

The  $^{19}\text{F}$  ENDOR spectra of the difluorinated compounds **2** and **3** and their simulations at 263 and 94 GHz are shown in Fig. 3, the contributions of each F atom are highlighted separately. As expected, the two different  $^{19}\text{F}$  nuclei of compound **2** are clearly distinguishable (see Fig. 3A, B) due to the different distances towards the paramagnetic centre. The contribution of the *o*-F atom of **2** is similar to the spectra of compound **1** (Fig. 2). The resonances belonging to the *m*-F nucleus are visible as shoulders inside of the main peaks due to the smaller HFC constant. Again, the strongest influence of the CSA of both  $^{19}\text{F}$  atoms of **2** on the spectrum is displayed at  $B_0 \parallel g_y$ . The contributions from parallel components of the HFC tensor, which are only resolved for the *o*-F nucleus at  $B_0 \parallel g_y$ , are clearly centred on a different frequency than the perpendicular components of the same nucleus. Furthermore, the perpendicular HFC component of the *m*-F atom is centred on a different frequency from that of the *o*-F atom, the difference amounts to  $\sim 20$  kHz, i.e. ca. 50 ppm. This reflects the influence of the CSA for the two atoms at this position. At the same observer position at 94 GHz, the chemical shift difference leads to a shift of  $\sim 7$  kHz for the two  $^{19}\text{F}$  nuclei, which is unresolved in the spectra (Fig. 3B). At the other positions,

the influence of the CSA is less apparent, in analogy to observations made on compound **1**.

Simulations using the parameters given in Table 1 reproduce the ENDOR spectra at both MW frequencies. The simulation parameters of the HFC of *m*-F are in good agreement with those of compound **6** published before [26]. The absolute CSA values of the *m*-F atom used in the simulations are larger than those reported previously for 2-F-Tyr derived by NMR [54], and also the values for the *o*-F atom in **2** exceed the values used in the case of compound **1**. This is most noteworthy for  $\delta_z$ , where absolute deviations of 50 – 60 ppm between our ENDOR derived and previously reported NMR values are observed for the two F atoms [18,54]. Here, we notice that the values used for simulation are taken from DFT calculations, indicating that the larger values have a physical origin and are not caused by experimental uncertainty. In fact, an increase of  $\delta_z$  compared to fluorobenzene [53] has been reported for the  $^{19}\text{F}$  atoms in 1,2-difluorobenzene, which has a vicinal difluoro-substitution pattern like **2**. This provides further support for the accuracy of our experimental  $\delta$  values and our interpretation of the rather large chemical shift values.

In case of the second difluorinated compound **3**, the contributions of the two  $^{19}\text{F}$  nuclei are not resolved as individual peaks in the experimental data (Fig. 3C, D) at either 263 or 94 GHz (Fig. 3C, D). The CSA affects the spectra in a similar fashion as observed in **1** and **2**. Again, good agreement between simulation and experiment was obtained. Comparing the spectra and simulation parameters of **3** to those of **1** reveals that the apparent splitting and also the used coupling constants are significantly smaller for the difluorinated model compound **3** (on average by 22 kHz, Table 1). The smaller dipolar coupling constants place the two  $^{19}\text{F}$  atoms in **3** at an average distance of 6.8 Å (calculated using Equation (9)) from the electron spin (Table 1), which exceeds the values obtained for **1** and **2** by 0.1 – 0.2 Å. The different splitting is caused by the presence of the second  $^{19}\text{F}$  atom in **3**, which corresponds to the minor contribution of conformation **1b** proposed in our previous study (Fig. 1B, D) [26]. The coupling constants for the two  $^{19}\text{F}$  atoms in **3** differ by only 25 kHz, meaning

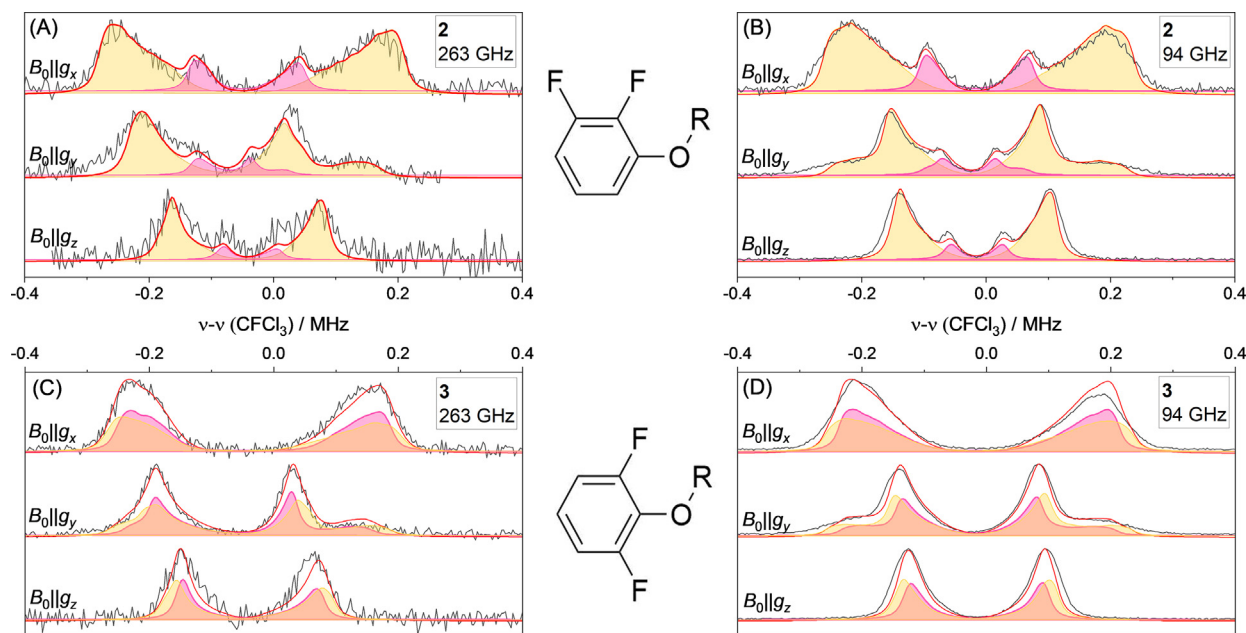


**Fig. 3.**  $^{19}\text{F}$  ENDOR spectra of compounds **2** and **3** at 263 GHz (A, C) and 94 GHz (B, D), all spectra measured at  $T = 50$  K. Experimental data are given in black, simulations in red. The individual contributions of the two F atoms in **2** and **3** are given in yellow and pink. Substitution schemes are given in the insets and all simulation parameters are listed in Table 1.

that the resulting HFC peaks would be separated by only  $\sim 13$  kHz (the HFC peaks appear at  $\pm T/2$  in the absence of CSA [26]), which is below the ENDOR line width of 20 kHz. The analysis shows that  $^{19}\text{F}$  ENDOR clearly allows distinguishing average distances differing by margins of only  $\sim 0.2$  Å in different samples (**1** vs **3**), but resolving two distances in one sample is only possible if the separation of peaks in a spectrum exceeds the ENDOR line width. Simulating the ENDOR spectrum with a single nucleus with unchanged line width parameter would result in ENDOR lines that are sharper than those observed experimentally (Figure S8). This observation highlights the value of accounting for the experimentally observed ENDOR line width to recover all information about electron- $^{19}\text{F}$  distances. In contrast to the hyperfine splitting, the CSA values of the F atoms are very similar in **3** and **1**. Consequently, the CSA values of **3** agree within our range of uncertainty with those reported previously for 3-F-Tyr [18,54], too, and difluorination in **3** does not affect  $\delta_z$  as strongly as in the vicinally substituted difluoro compound **2**.

Fig. 4 shows the experimental and simulated ENDOR spectra of the  $\text{CF}_3$  substituted compounds **4** and **5**. In the spectra of **4** (Fig. 4A, B) three different HFC contributions are resolved both at 263 and 94 GHz, indicating that the  $\text{CF}_3$  group is not rotating on the timescale of the ENDOR experiment ( $\sim$ length of the RF pulse, 50  $\mu\text{s}$ ) at 50 K. According to DFT calculations, the dipolar coupling constants differ by more than 60 kHz for the three  $^{19}\text{F}$  atoms, which would place their ENDOR resonances at positions separated by more than 30 kHz in the absence of CSA contributions. This separation exceeds the ENDOR line width observed herein and in our previous study [26], and thus resolution of the features is expected. Concordantly, the spectra at both MW frequencies clearly resolve features originating from different  $^{19}\text{F}$  nuclei.

The separation of features is of course also influenced by the contributions of the CSA, meaning that the number of resolved peaks might be diminished for specific combinations of HFC and CSA parameters. At 263 GHz, clear asymmetry owed to CSA contributions is observed at all three observer positions. Interestingly, the observed asymmetry is also notable at 94 GHz: Three peaks at the high frequency side but only two at the low frequency side are resolved at  $B_0 \parallel g_y$ , and vice versa at  $B_0 \parallel g_z$ . Given that the differ-

ences in HFC are barely above the resolution limit, the small influence of the CSA at 94 GHz already suffices to produce asymmetric spectra that require consideration of CSA contributions even for a qualitative understanding. Considering the complexity of the spectra of **4**, it is clear that a reliable analysis is only possible by simulation. Using the parameters listed in Table 1 allows explaining the observed asymmetry at both MW frequencies.

Spectral simulation in the case of **4** required using a DFT model, whereas a reliable, model-free fit of all 27 parameters (six CSA and three HFC parameters per  $^{19}\text{F}$  atom) is deemed impossible. However, the resolution obtained at both MW frequencies would certainly allow extracting the HFC constants for all  $^{19}\text{F}$  atoms even without DFT model. Furthermore, the CSA of the two atoms with larger HFC constants could also be analysed to some extent. In contrast, the CSA of the most weakly coupled  $^{19}\text{F}$  nucleus is not sufficiently resolved to be analysed without DFT model. We note, that DFT predicts different CSA principal values for the three atoms of the  $\text{CF}_3$  group, which are chemically identical. Comparing the ENDOR derived CSA values with previously published NMR data is complicated by the fact that the  $\text{CF}_3$  group in **4** is static on the timescale of the ENDOR experiment at 50 K. In contrast, uniaxial rotation occurred in the NMR study by Grage *et al.* [42], who reported the partially averaged CSA tensors of nine trifluoromethylated compounds. The reported isotropic values of these compounds span a range of  $-60$  to  $-87$  ppm, which agrees within our experimental uncertainty with the  $\delta_{\text{iso}}$  values of the  $^{19}\text{F}$  atoms in **4** reported in Table 1.

In case of *p*- $\text{CF}_3$  substituted **5**, only a single peak doublet is resolved at all observer position at both MW frequencies at 50 K (Fig. 4C, D), our standard temperature for measurements on nitroxides. Consequently, the spectra could be simulated with a single HFC tensor and an isotropic chemical shift of  $-75$  ppm, within uncertainty identical to the  $\delta_{\text{iso}}$  values of **4**. We note, that  $\delta_{\text{iso}}$  of the  $\text{CF}_3$  group in **4** and **5** appears to be hardly affected by its position in the aromatic ring. This finding is in agreement with the reported isotropic  $\delta_{\text{iso}}$  values of *o*-, *m*- and *p*- $\text{CF}_3$ -phenol, which differ by only about 2 ppm [50]. When the complete, DFT derived CSA tensors are used, different line shapes are obtained, inconsistent with the experimental spectra at 50 K (see Figure S9 A in the SI).

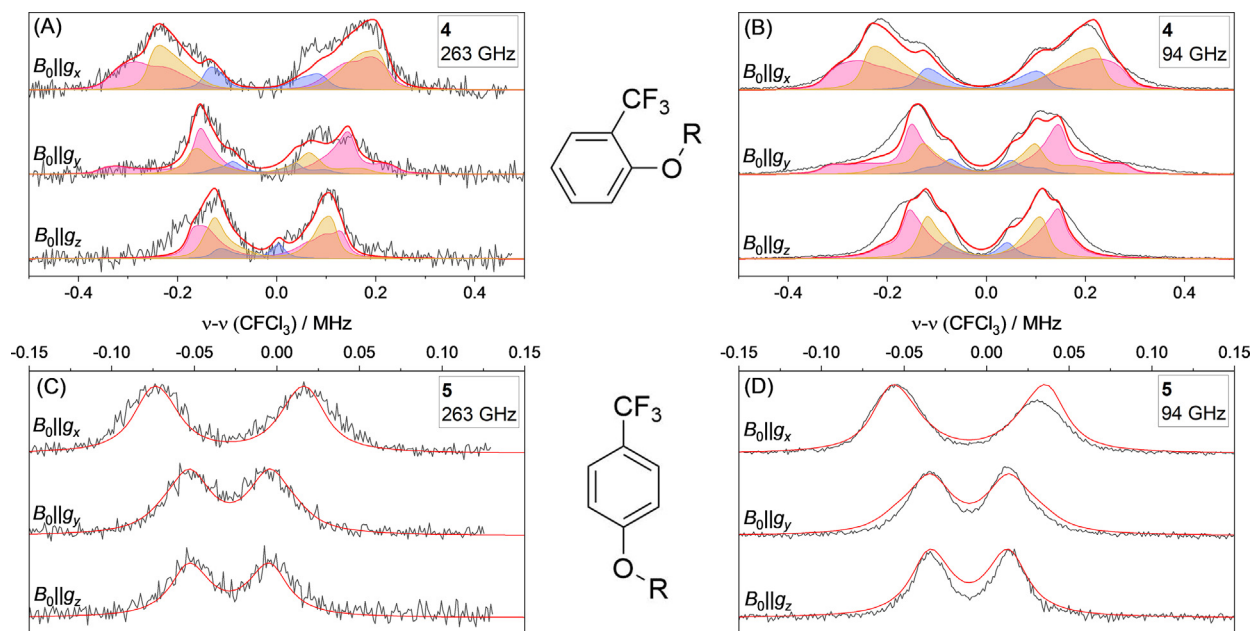


**Fig. 4.**  $^{19}\text{F}$  ENDOR spectra of compounds **4** and **5** at 263 GHz (A, C) and 94 GHz (B, D), all spectra measured at  $T = 50$  K. Experimental data are given in black, simulations in red. The individual contributions of the F atoms in **4** are given in yellow, pink and blue. Substitution schemes are given in the insets and all simulation parameters are listed in Table 1.

Even though no rotation was observed in the case of the *o*- $\text{CF}_3$  group in **4**, one explanation for this effect could be rapid rotation of the *p*- $\text{CF}_3$  group in **5**, which would lead to partial averaging of the CSA tensors. Since the local environments of the  $\text{CF}_3$  group in **4** and **5** are different due to the vicinity of the carboxylate group in **4**, different rotational behaviour cannot be excluded. Indeed, DFT calculations predict strongly different rotational barriers of  $\sim 30$  and  $\sim 3$  kJ/mol for **4** and **5**, respectively (see Figure S9 B). Furthermore, when repeating the 9.4 T/263 GHz ENDOR experiment at 10 K, asymmetric features are observed in the spectra of **5**. These features are also present in the simulations using the complete, non-averaged CSA tensors predicted by DFT (Figure S10).

### 3. Summary and conclusions

In this work we demonstrated that the CSA visibly affects the 263 GHz  $^{19}\text{F}$  ENDOR spectra of compounds **1** – **5** by introducing a pronounced asymmetry, if no dynamical averaging of the CSA occurs. Despite this observation, the HFC dominated the line shape of all reported ENDOR spectra. The influence of the CSA was best observed for nuclei which also had relatively large HFC constants, as this spreads out the observed resonances over a large frequency range and thereby effectively increases the spectral resolution. We observed that the CSA of the weakly coupled  $^{19}\text{F}$  nuclei in **2** (with  $T \approx 90$  kHz) and **4** ( $T \approx 130$  kHz) was not clearly resolved because of overlap with resonances originating from the more strongly coupled nuclei. Obtaining the CSA tensor and its orientation within the molecular frame provides further constraints for modelling in structural biology applications. Compound **5** differs from **1** to **4**, as it was not possible to obtain detailed information about either the CSA or the HFC tensor of individual atoms at 50 K in this example. However, CSA visibly affects the ENDOR spectra of **5** at 10 K, where it was possible to resolve resonances originating from individual  $^{19}\text{F}$  nuclei with different effective chemical shifts. This observation suggests that rapid, uniaxial rotation of the *p*- $\text{CF}_3$  group occurs at temperatures as low as 50 K, leading to partial averaging of the CSA. This interpretation is supported by DFT cal-

culations, which predict a rotational barrier of only ca. 3 kJ/mol for the *p*- $\text{CF}_3$  group in **5**. Notably, the HFC constants of the three  $^{19}\text{F}$  atoms in **5** differ by only ca. 2 kHz, which is below the resolution limit. Consequently, only the ability to resolve the CSA enabled probing the dynamical behaviour of the  $\text{CF}_3$  group in **5** using ENDOR spectroscopy.

The ENDOR resolution in case of stronger couplings will often be lower than the resolution that was achieved herein and in our previous study [26], as inhomogeneous broadening is expected to become more impactful for strongly coupled nuclei. In the context of ENDOR based distance measurements using  $^{19}\text{F}$  nuclear spin labels in structural biology, such high resolution is achieved by engineering weak HFC interactions and avoiding overlap with resonances from other nuclei, which was also demonstrated using  $^{31}\text{P}$  nuclei [55]. The ENDOR line width is an important determinant for the ability to resolve the CSA. Conversely, it is also important to understand the effect of the CSA on the inhomogeneous line width, which can in principle be used to derive distance distributions from the ENDOR data, as demonstrated in a recent study [56].

Aside from its effect on the ENDOR linewidth, the influence of the CSA is reduced and can be neglected in many cases for  $^{19}\text{F}$  nuclei at 3.4 T/94 GHz, albeit the spectra of compound **4** revealed notable asymmetries even at this field. Thus, the ability of extracting CSA information appears mostly restricted to the – from the perspective of EPR spectroscopy – ‘very-high field case’ of 9.4 T. EPR spectroscopy at 263 GHz/9.4 T is still a niche and only a few instruments exist worldwide with this capability. Nonetheless, spectrometer technology is well-established and knowledge on attainable information, as we report here, is important to further develop and establish the method for many applications. Particularly, considering recent developments in  $^{19}\text{F}$  NMR as well as in DNP enhanced NMR, ENDOR in this frequency/field range might provide unprecedented synergy to modern NMR spectroscopy.

Aside from the applied magnetic field, another major factor determining the influence of the CSA is the type of nucleus that is observed, with heavier nuclei generally leading to larger CSAs. Thus, the presented results might also be relevant for applications in inorganic chemistry and transition metal catalysis, where HFC

analysis has been used in recent publications to provide insight into structures and mechanisms involving species that contain  $^{25}\text{Mg}$  [57],  $^{27}\text{Al}$  [58,59],  $^{29}\text{Si}$  [57,60],  $^{47/49}\text{Ti}$  [57–59], etc.

#### 4. Material and methods

**Syntheses.** Compounds **2** – **5** were synthesized and purified analogously to compound **1** [26], with typical yields of 60 – 70 %. Crystals for X-ray structure determination were obtained by slow evaporation of a solvent mix of dichloromethane and hexane. The identity of the compounds was confirmed by X-ray structure determination (CCDC numbers 2117608 - 2117611) and by ESI mass spectrometry. The purity of the compounds was confirmed by elemental analysis and HPLC (see chapter 3 of the SI).

Compound **2** ESI-MS:  $m/z$  319.1 (100%,  $[\text{C}_{15}\text{H}_{16}\text{F}_2\text{NO}_3\text{Na}]^+$ ,  $[\text{M} + \text{Na}]^+$ ), 297.1 (50%,  $[\text{C}_{15}\text{H}_{17}\text{F}_2\text{NO}_3]^+$ ),  $[\text{M} + \text{H}]^+$ , 296.1 (60%,  $[\text{C}_{15}\text{H}_{16}\text{F}_2\text{NO}_3]^+$ ,  $[\text{M}]^+$ ), 282.1 (100%,  $[\text{C}_{14}\text{H}_{14}\text{F}_2\text{NO}_3]^+$ ,  $[\text{M} - \text{CH}_2]^+$ ); Elemental Analysis: Calc.: C, 60.81; H, 5.44; N 4.73. Found: C, 60.61; H, 5.59; N, 4.89.

Compound **3** ESI-MS:  $m/z$  297.1 (50%,  $[\text{C}_{15}\text{H}_{17}\text{F}_2\text{NO}_3]^+$ ,  $[\text{M} + \text{H}]^+$ ), 296.1 (90%,  $[\text{C}_{15}\text{H}_{16}\text{F}_2\text{NO}_3]^+$ ,  $[\text{M}]^+$ );

Elemental Analysis: Calc.: C, 60.81; H, 5.44; N 4.73. Found: C, 61.04; H, 5.65; N, 4.77.

Compound **4** ESI-MS:  $m/z$  329.1 (7%,  $[\text{C}_{16}\text{H}_{18}\text{F}_3\text{NO}_3]^+$ ,  $[\text{M} + \text{H}]^+$ ), 328.1 (70%,  $[\text{C}_{16}\text{H}_{17}\text{F}_3\text{NO}_3]^+$ ,  $[\text{M}]^+$ ), 314.1 (100%,  $[\text{C}_{15}\text{H}_{15}\text{F}_3\text{NO}_3]^+$ ,  $[\text{M} - \text{CH}_2]^+$ ); Elemental Analysis: Calc.: C, 58.53; H, 5.22; N 4.27. Found: C, 58.55; H, 5.30; N, 4.28.

Compound **5** ESI-MS:  $m/z$  329.1 (15%,  $[\text{C}_{16}\text{H}_{18}\text{F}_3\text{NO}_3]^+$ ,  $[\text{M} + \text{H}]^+$ ), 328.1 (100%,  $[\text{C}_{16}\text{H}_{17}\text{F}_3\text{NO}_3]^+$ ,  $[\text{M}]^+$ ), 314.1 (8%,  $[\text{C}_{15}\text{H}_{15}\text{F}_3\text{NO}_3]^+$ ,  $[\text{M} - \text{CH}_2]^+$ ); Elemental Analysis: Calc.: C, 58.53; H, 5.22; N 4.27. Found: C, 58.47; H, 5.29; N, 4.27.

**94 GHz EPR/ENDOR spectroscopy.** The samples for EPR spectroscopy were prepared in Suprasil EPR tubes (Wilma LabGlass, 0.5 mm inner diameter (ID), 0.9 mm outer diameter (OD), open at both ends) at concentrations of  $c = 300 \mu\text{M}$  in a mixture of deuterated DMSO  $d_6$  and  $\text{CD}_3\text{OD}$  ( $v/v = 40/60$ ). Measurements were performed on an Elexsys E680 EPR spectrometer (Bruker BioSpin) equipped with a commercial, cylindrical TE<sub>011</sub>-mode EPR/ENDOR resonator (EN600-1021H, Bruker BioSpin) inserted into a helium gas flow cryostat (Oxford Instruments). Using a 2 W MW amplifier, typical  $\pi/2$  pulse lengths of 10 – 12 ns were achieved. EPR spectra were recorded using a two-pulse echo sequence ( $\pi/2 - \tau - \pi - \tau$ -echo) and a delay time  $\tau = 240$  ns. A linearization procedure implemented by Bruker BioSpin was used to compensate non-linear behaviour of the magnetic field during the sweep. For Mims ENDOR ( $\pi/2 - \tau - \pi/2 - t_{\text{RF}} - \pi/2 - \tau$ -echo) measurements, the MW power was attenuated to increase the  $\pi/2$  pulse lengths to 30 – 34 ns to make the measurement conditions more similar to the conditions used at 263 GHz. The length of the delay time  $\tau$  was set to 850 ns for compounds **1** – **4**. For compound **5** the delay time  $\tau$  was set to 2000 ns to account for the smaller HFC in **5**. RF pulses were amplified with a 250 W RF amplifier (250A250A Amplifier Research). RF  $\pi$  pulse lengths of 50  $\mu\text{s}$  were used (optimized performing Rabi nutation experiments). ENDOR spectra were recorded using stochastic RF acquisition with 10 shots-per-point and a shot-repetition-time of 4 ms. Typical acquisition times amounted to  $\leq 6$  h ( $B_0 \parallel g_x$  and  $g_y$ ) and  $\sim 12$  h ( $B_0 \parallel g_z$ ). To keep track of possible experimental drifts, the  $^{19}\text{F}$  ENDOR experiments were conducted in batches, which means that the spectra were recorded in two-dimensional data sets of size  $B \times N$ , where  $B$  is the number of batches and  $N$  is the number of points on the frequency axis [35]. All spectra were recorded at 50 K. Further details are tabulated in the SI.

**263 GHz EPR/ENDOR spectroscopy.** The samples were prepared as described for the 94 GHz samples using Vitrocom capillar-

ies CV2033S/Q (ID 0.2 mm, OD 0.33 mm, open at both ends). Measurements were performed on an Elexsys E780 spectrometer (Bruker BioSpin) equipped with a cylindrical TE<sub>012</sub>-mode EPR/ENDOR resonator (E950110, Bruker BioSpin) inserted into a helium gas flow cryostat (Oxford Instruments). All experiments were performed at 50 K. A 100 mW amplifier-multiplier-chain (Virginia Diodes) coupled to the resonator via a corrugated waveguide achieved  $\pi/2$  pulse lengths of 32 – 40 ns.

EPR spectra were recorded using a two-pulse echo sequence ( $\pi/2 - \tau - \pi - \tau$ -echo) and a delay time  $\tau = 300$  ns. A linearization procedure implemented by Bruker BioSpin was used to compensate non-linear behaviour of the magnetic field during the sweep. Mims ENDOR spectra were recorded using the same  $\tau$  values for compounds **1** – **5** as in the measurements at 94 GHz. The RF irradiation was amplified by a 125 W amplifier (model 125 W1000, Amplifier Research). The RF pulse length was set to 50  $\mu\text{s}$ , which was determined by performing Rabi-nutation experiments. All ENDOR spectra at 263 GHz were recorded with stochastic acquisition and a shot repetition time of 3 ms. The acquisition time per spectrum was between 2 and 21 h, depending on sample and field position (details are given in Table S1). Similar to the procedure at 94 GHz, ENDOR data were recorded in batches [35]. All spectra shown in the main text were obtained at 50 K, spectra of **5** obtained at 10 K are shown in Figure S10. Further details on the spectrometer setup are provided in a previous publication [34].

**Data processing and  $^{19}\text{F}$  frequency referencing.** During data processing, the ENDOR spectra in all individual batches were summed up first (standard averaging), and second, a phase correction was applied in order to maximize the real part of the spectrum. A first order polynomial baseline correction was applied and the spectra were normalized to the largest absolute ENDOR intensity. Finally, the spectra were referenced to the  $^{19}\text{F}$  resonance frequency of  $\text{CFCl}_3$  by subtracting  $\nu_{\text{ref}}(\text{CFCl}_3)$  from the ENDOR RF axis (Equations (6) and (7)). To determine  $\nu_{\text{ref}}(\text{CFCl}_3)$  from Equation (7),  $^1\text{H}$  ENDOR spectra were recorded at each considered position in the EPR line and  $\nu_{\text{H},0}$  was determined from the center of these spectra, as they were symmetric around  $\nu_{\text{H},0}$  (i.e. no  $^1\text{H}$  CSA was resolved). Moreover, we approximated  $\nu_{\text{H},0} \approx \nu_{\text{H}}(\text{TMS})$  in Equation (7), as the CSA of  $^1\text{H}$  is typically small ( $<30$  ppm, i.e.  $<12$  kHz at 9.4 T). The available ENDOR resolution and the neglect of  $^1\text{H}$  chemical shift introduce an estimated uncertainty of 20 – 30 ppm for the chemical shifts derived from the 263 GHz  $^{19}\text{F}$  ENDOR spectra.

Because of the importance of the factor  $\Xi$  in Eq. (7), we examined the origin of its numerical value. When employing  $g_n(^1\text{H}) = 5.58569468$  and  $g_n(^{19}\text{F}) = 5.257736$  from Stone (IAEA Table [45,61]) and shielding values in the range of  $\sigma_{\text{iso}}(\text{TMS}) \approx 30$  ppm (value from our DFT calculation, in agreement with value reported by Makulski and Jackowski [62]) as well as  $\sigma_{\text{iso}}(\text{CFCl}_3) \approx 160 - 195$  ppm (160 ppm from our DFT, 195 ppm from Jameson *et al.* [63]) we arrived at  $\Xi \approx 0.94113 - 0.94116$ , which exceeds the recommended IUPAC  $\Xi$  value by about  $2 \cdot 10^{-4}$ , i.e. 200 ppm. A closer inspection of the literature revealed that there seems to be a discrepancy on the reported  $^{19}\text{F}$  nuclear  $g$  factors. Based on gas phase NMR measurements, lower values for  $g_n(^{19}\text{F})$  were obtained in studies by Baker *et al.* [64] and by Jaszúnski *et al.* [65]. Using  $g_n(^{19}\text{F}) = 5.25667$ , which is the average of the values proposed in refs. 64 and 65, we arrive at  $\Xi \approx 0.94094 - 0.94097$ , which basically reproduces to the IUPAC  $\Xi$  value.

We also applied the recently presented drift model [35], but no significant gain in the signal-to-noise ratio was obtained as compared to the standard averaging, because only minor signal drifts were observed throughout the measurements. Since statistical analysis of the spectral uncertainty goes beyond the scope of the

work presented here, all presented spectra result from direct averaging. However, developments for obtaining the uncertainties of  $^{19}\text{F}$  tensor parameters from the spectral confidence intervals are ongoing.

**ENDOR spectral simulations.** The simulation of the ENDOR spectra is performed in two major steps. First, the nitroxide's EPR spectrum is simulated to preselect orientations that contribute to the ENDOR spectrum (Figure S1). For this step, the electronic part of the spin Hamiltonian including the  $^{14}\text{N}$  HFC coupling, denoted  $\hat{H}_{\text{S,EPR}}$  in Eq. (1) and detailed in Eq. (2), is diagonalized as explained in the theory section for each set of Euler angles  $\theta$  and  $\varphi$  describing the orientation of the  $g$  principal axes into the laboratory frame. For fast computation, this Hamiltonian is treated as an effective  $S = 1/2$  coupled to a  $I = 1$  spin system ( $6 \times 6$  matrix), neglecting the much smaller  $^{19}\text{F}$  couplings which are within the EPR line width. After diagonalization of  $\hat{H}_{\text{S,EPR}}$ , all possible ESR transitions between the six quantum states are considered, according to their transition probabilities. Representative computations of these transitions and their probabilities for individual orientations are illustrated in Figures S2 – S4 and were verified by an *EasySpin* [66] calculation. In both programs, identical EPR parameters were used ( $g_x = 2.00913$ ,  $g_y = 2.00633$ ,  $g_z = 2.00233$ ,  $A_{x,1} = A_{y,1} = 13$  MHz,  $A_{z,1} = 94$  MHz,  $P_{x,1} = 1.3$  MHz,  $P_{y,1} = 0.5$  MHz, and  $P_{z,1} = -1.8$  MHz for the  $\mathbf{g}$ ,  $\mathbf{A}_1$ , and  $\mathbf{P}_1$  matrices, respectively). Indeed, it is shown that at several orientations, the EPR forbidden transitions become allowed due to the strong anisotropy of the  $^{14}\text{N}$  nitroxide HFC, which exceeds the  $^{14}\text{N}$  Larmor frequency ( $\sim 29$  MHz) at 263 GHz/9.4 T.

In the next step, the molecular orientations contributing to the ENDOR spectrum are computed according to the MW resonance and excitation bandwidth within the EPR line, as previously described [34]. The  $^{19}\text{F}$  ENDOR transitions energies are calculated from Eqs. (3) – (6) for each pre-selected molecular orientation, corresponding to a pair of Euler angles  $\theta$  and  $\varphi$ . The elements of the  $^{19}\text{F}$  HFC and CSA tensors in the laboratory frame are obtained by performing Euler rotations. Taking the HFC tensor as an example, the first step transforms  $\mathbf{A}$  into the  $\mathbf{g}$  principal axis frame using the Euler angles  $\alpha^{\text{HFC}}$ ,  $\beta^{\text{HFC}}$  and  $\gamma^{\text{HFC}}$  and second, into the laboratory frame using the rotational matrices  $R_\theta$  and  $R_\varphi$ :  $\mathbf{A}^{\text{diag}} \xrightarrow{R_{\alpha^{\text{HFC}}, \beta^{\text{HFC}}, \gamma^{\text{HFC}}}} \mathbf{A}^{\mathbf{g}} \xrightarrow{R_{\theta, \varphi}} \mathbf{A}^{\text{lab}}$ . Finally,  $A_{zz}$  is extracted from  $\mathbf{A}^{\text{lab}}$ . An analogous procedure is performed to calculate  $\sigma_{zz}$ .

Each computed ENDOR transition is weighted by a numerical factor  $F$  that is calculated by the Mims blind spot function, depending on  $A_{zz}$  and the inter-pulse separation of the first two MW-pulses  $\tau$  (Eq. (10)) [22]:

$$F = 0.5 \cdot \sin^2\left(2\pi \frac{A_{zz}}{2} \tau\right) \quad (10)$$

Finally, all contributions of individual ENDOR transitions are summed up and convolved with a line broadening function (Lorentzian), as previously reported [29,34]. A comparison between ENDOR simulations performed with the here described method and *EasySpin* is presented in SI 1.4 (Figure S7) for 94 GHz. We note that *EasySpin* does not include CSA, therefore a further comparison of simulations at 263 GHz is not feasible.

For the simulation strategy, the chemical shift principal values of compounds **1** – **5** and  $\text{CFCl}_3$  for referencing were predicted by DFT calculations. The DFT derived CSA parameters were kept fixed within 3 ppm in the ENDOR simulations. The Euler angles between CSA and  $g$  tensor were also taken from DFT and adjusted within a few degrees ( $<10^\circ$ ).  $^{19}\text{F}$  HFCs were first simulated with the 94 GHz ENDOR spectra, starting from the DFT predicted values, and then iteratively optimized to reproduce also the 263 GHz ENDOR spectra.

**DFT calculations.** All DFT calculations were performed with ORCA 4.2.1 [67]. For geometry optimizations the B3LYP functional [68–71] with tight SCF convergence criteria, the def2-TZVPP basis set [72] and Grimme's dispersion correction with the Becke-Johnson damping scheme (D3BJ) [73,74] were used. For NMR property calculations gauge-independent atomic orbital (GIAO)-DFT calculations using the PBE0 functional [75,76] and the def2-TZVPP basis sets [72] with the auxiliary basis set def2/JK [77] and RIJK approximation for the NMR property calculations [78,79] were performed. For EPR property calculations, the EPR-II basis set [80] and the B3LYP functional [68–71] were used. For the dihedral scan (compounds **4** and **5**, Figure S9 B) the respective dihedral angle was varied in  $10^\circ$  steps and for each step a constrained geometry optimization was performed.

## Declaration of Competing Interest

The authors declare that they have no known competing financial interests or personal relationships that could have appeared to influence the work reported in this paper.

## Acknowledgements

Gordian Sandberg is gratefully acknowledged for the synthesis and crystallisation of **5**. We thank Prof. Dr. Franc Meyer for providing access to the X-ray facilities at the University of Göttingen and Manuel Oelschlegel for collecting the X-ray diffraction data of **2**. Dr. Michael John is gratefully acknowledged for discussing the factor  $\Xi$  with us and for his comments on the theory section. Financial support by the Max Planck Society is gratefully acknowledged. AK acknowledges financial support by the IMPRS-PBCS of the Max Planck Society. AK, MH, and MB acknowledge support by the SFB 1456 of the Deutsche Forschungsgemeinschaft (DFG). This project has been partially funded by the DFG project number 423268549 (INST 186/1327-1 FUGG) and the Nds. Ministerium für Wissenschaft und Kultur.

## Appendix A. Supplementary material

Supplementary data to this article can be found online at <https://doi.org/10.1016/j.jmr.2021.107091>. Original spectroscopic and crystallographic data can be found at <https://data.goettingen-research-online.de/dataset.xhtml?persistentId=doi:10.25625/FLQKPM>.

## References

- [1] V. Gouverneur, *Fluorine in Pharmaceutical and Medicinal Chemistry: from biophysical aspects to clinical applications*, World Scientific, 2012.
- [2] S.L. Cobb, C.D. Murphy,  $^{19}\text{F}$  NMR applications in chemical biology, *J. Fluorine Chem.* 130 (2009) 132–143.
- [3] H. Chen, S. Viel, F. Ziarelli, L. Peng,  $^{19}\text{F}$  NMR: a valuable tool for studying biological events, *Chem. Soc. Rev.* 42 (2013) 7971–7982.
- [4] E.N.G. Marsh, Y. Suzuki, Using  $^{19}\text{F}$  NMR to Probe Biological Interactions of Proteins and Peptides, *ACS Chem. Biol.* 9 (2014) 1242–1250.
- [5] J. Ruiz-Cabello, B.P. Barnett, P.A. Bottomley, J.W.M. Bulte, Fluorine ( $^{19}\text{F}$ ) MRS and MRI in biomedicine, *NMR Biomed.* 24 (2011) 114–129.
- [6] A. Divakaran, S.E. Kirberger, W.C.K. Pomerantz, SAR by (Protein-Observed)  $^{19}\text{F}$  NMR, *Acc. Chem. Res.* 52 (2019) 3407–3418.
- [7] J.L. Kiteviski-LeBlanc, R.S. Prosser, Current applications of  $^{19}\text{F}$  NMR to studies of protein structure and dynamics, *Prog. Nucl. Magn. Reson. Spectrosc.* 1–33 (2012).
- [8] K.E. Arntson, W.C.K. Pomerantz, Protein-Observed Fluorine NMR: A Bioorthogonal Approach for Small Molecule Discovery, *J. Med. Chem.* 59 (2016) 5158–5171.
- [9] M. Salwiczek, E.K. Nyakatura, U.I.M. Gerling, S. Ye, B. Koksich, Fluorinated amino acids: compatibility with native protein structures and effects on protein–protein interactions, *Chem. Soc. Rev.* 41 (2012) 2135–2171.
- [10] H. Welte, T. Zhou, X. Mihajlenko, O. Mayans, M. Kovermann, What does fluorine do to a protein? Thermodynamic, and highly-resolved structural

- insights into fluorine-labelled variants of the cold shock protein, *Sci. Rep.* 10 (2020) 2640.
- [11] M. Wang, M. Lu, M.P. Fritz, C.M. Quinn, I.-J.-L. Byeon, C.-H. Byeon, J. Struppe, W. Maas, A.M. Gronenborn, T. Polenova, Fast Magic-Angle Spinning  $^{19}\text{F}$  NMR Spectroscopy of HIV-1 Capsid Protein Assemblies, *Angew. Chem. Int. Ed.* 57 (2018) 16375–16379.
  - [12] S. Wi, N. Sinha, M. Hong, Long-Range  $^1\text{H}$ - $^{19}\text{F}$  Distance Measurement in Peptides by Solid-State NMR, *J. Am. Chem. Soc.* 126 (2004) 12754–12755.
  - [13] M. Roos, V.S. Mandala, M. Hong, Determination of Long-Range Distances by Fast Magic-Angle-Spinning Radiofrequency-Driven  $^{19}\text{F}$ - $^{19}\text{F}$  Dipolar Recoupling NMR, *J. Phys. Chem. B.* 122 (2018) 9302–9313.
  - [14] E. Matei, A.M. Gronenborn,  $^{19}\text{F}$  Paramagnetic Relaxation Enhancement: A Valuable Tool for Distance Measurements in Proteins, *Angew. Chem. Int. Ed.* 55 (2016) 150–154.
  - [15] K. Zimmermann, D. Joss, T. Müntener, E.S. Nogueira, M. Schäfer, L. Knörr, F.W. Monnard, D. Häussinger, Localization of ligands within human carbonic anhydrase II using  $^{19}\text{F}$  pseudocontact shift analysis, *Chem. Sci.* 10 (2019) 5064–5072.
  - [16] W.R. Dolbier Jr, Guide to fluorine NMR for organic chemists, John Wiley & Sons, 2016.
  - [17] R. Zhang, K.H. Mroue, A. Ramamoorthy, Proton-Based Ultrafast Magic Angle Spinning Solid-State NMR Spectroscopy, *Acc. Chem. Res.* 50 (2017) 1105–1113.
  - [18] U.H.N. Dürr, S.L. Grage, R. Witter, A.S. Ulrich, Solid state  $^{19}\text{F}$  NMR parameters of fluorine-labeled amino acids. Part I: Aromatic substituents, *J. Magn. Reson.* 191 (2008) 7–15.
  - [19] C. Dalvit, A. Vulpetti, Ligand-Based Fluorine NMR Screening: Principles and Applications in Drug Discovery Projects, *J. Med. Chem.* 62 (2019) 2218–2244.
  - [20] T.H. Kim, P. Mehrabi, Z. Ren, A. Sjöka, C. Ing, A. Bezinov, L. Ye, R. Pomès, R.S. Prosser, E.F. Pai, The role of dimer asymmetry and protomer dynamics in enzyme catalysis, *Science*, 355 (2017) eaag2355.
  - [21] B.J. Dow, S.S. Malik, A.C. Drohat, Defining the Role of Nucleotide Flipping in Enzyme Specificity Using  $^{19}\text{F}$  NMR, *J. Am. Chem. Soc.* 141 (2019) 4952–4962.
  - [22] J. Harmer, Hyperfine Spectroscopy - ENDOR, in: D. Goldfarb, S. Stoll (Eds.), *EPR Spectroscopy: Fundamentals and Methods*, Wiley, 2018, pp. 331–358.
  - [23] G.B. Wells, M.W. Makinen, ENDOR Determined Molecular Geometries of Spin-Labeled Fluoroanilides in Frozen Solution, *J. Am. Chem. Soc.* 110 (1988) 6343–6352.
  - [24] F. Jiang, S.-W. Tsai, S. Chen, M.W. Makinen, ENDOR Determined Structure of a Complex of  $\alpha$ -Chymotrypsin with a Spin-Labeled Transition-State Inhibitor Analogue, *J. Phys. Chem. B.* 102 (1998) 4619–4627.
  - [25] W.B. Mims, Pulsed endor experiments, *Proc. R. Soc. Lond. A* 283 (1965) 452–457.
  - [26] A. Meyer, S. Dechert, S. Dey, C. Höbartner, M. Bennati, Measurement of Angstrom to Nanometer Molecular Distances with  $^{19}\text{F}$  Nuclear Spins by EPR/ENDOR Spectroscopy, *Angew. Chem. Int. Ed.* 59 (2020) 373–379.
  - [27] B.L. Greene, G. Kang, C. Cui, M. Bennati, D.G. Nocera, C.L. Drennan, J. Stubbe, Ribonucleotide Reductases: Structure, Chemistry, and Metabolism Suggest New Therapeutic Targets, *Annu. Rev. Biochem.* 89 (2020) 45–75.
  - [28] C.W. Hoganson, M. Sahlin, B.-M. Sjöberg, G.T. Babcock, Electron Magnetic Resonance of the Tyrosyl Radical in Ribonucleotide Reductase from *Escherichia coli*, *J. Am. Chem. Soc.* 118 (1996) 4672–4679.
  - [29] M. Bennati, C.T. Farrar, J.A. Bryant, S.J. Inati, V. Weis, G.J. Gerfen, P. Riggs-Gelasco, J. Stubbe, R.G. Griffin, Pulsed Electron-Nuclear Double Resonance (ENDOR) at 140 GHz, *J. Magn. Reson.* 138 (1999) 232–243.
  - [30] B.A. Diner, Amino acid residues involved in the coordination and assembly of the manganese cluster of photosystem II. Proton-coupled electron transport of the redox-active tyrosines and its relationship to water oxidation, *Biochim. Biophys. Acta* 1503 (2001) 147–163.
  - [31] A.W. Rutherford, A. Boussac, P. Fallor, The stable tyrosyl radical in Photosystem II: why D?, *Biochim. Biophys. Acta* 1655 (2004) 222–230.
  - [32] I. Pujols-Ayala, B.A. Barry, Tyrosyl radicals in Photosystem II, *Biochim. Biophys. Acta* 1655 (2004) 205–216.
  - [33] K. Warncke, J. McCracken, G.T. Babcock, Structure of the YD Tyrosine Radical in Photosystem II as Revealed by  $^2\text{H}$  Electron Spin Echo Envelope Modulation (ESEEM) Spectroscopic Analysis of Hydrogen Hyperfine Interactions, *J. Am. Chem. Soc.* 116 (1994) 7332–7340.
  - [34] I. Tkach, I. Bejenke, F. Hecker, A. Kehl, M. Kasanmascheff, I. Gromov, I. Prisecaru, P. Höfer, M. Hiller, M. Bennati,  $^1\text{H}$  high field electron-nuclear double resonance spectroscopy at 263 GHz/9.4 T, *J. Magn. Reson.* 303 (2019) 17–27.
  - [35] Y. Pokern, B. Eltzner, S.F. Huckemann, C. Beeken, J. Stubbe, I. Tkach, M. Bennati, M. Hiller, Statistical analysis of ENDOR spectra, *Proc. Natl. Acad. Sci.* 118 (2021) e2023615118, <https://doi.org/10.1073/pnas.2023615118>.
  - [36] M. Hiller, I. Tkach, H. Wiechers, B. Eltzner, S. Huckemann, Y. Pokern, M. Bennati, Distribution of  $\text{H}^\beta$  Hyperfine Couplings in a Tyrosyl Radical Revealed by 263 GHz ENDOR Spectroscopy, *Appl. Magn. Reson.* (2021), <https://doi.org/10.1007/s00723-021-01411-5>.
  - [37] F. Hecker, J. Stubbe, M. Bennati, Detection of Water Molecules on the Radical Transfer Pathway of Ribonucleotide Reductase by  $^{17}\text{O}$  Electron-Nuclear Double Resonance Spectroscopy, *J. Am. Chem. Soc.* 143 (2021) 7237–7241.
  - [38] M.H. Levitt, Spin dynamics: basics of nuclear magnetic resonance, John Wiley & Sons, 2013.
  - [39] S.L. Grage, A.S. Ulrich, Orientation-Dependent  $^{19}\text{F}$  Dipolar Couplings within a Trifluoromethyl Group Are Revealed by Static Multipulse NMR in the Solid State, *J. Magn. Reson.* 146 (2000) 81–88.
  - [40] R.W. Glaser, C. Sachse, U.H.N. Dürr, P. Wadhvani, A.S. Ulrich, Orientation of the antimicrobial peptide PGLa in lipid membranes determined from  $^{19}\text{F}$ -NMR dipolar couplings of 4- $\text{CF}_3$ -phenylglycine labels, *J. Magn. Reson.* 168 (2004) 153–163.
  - [41] K.M. Sharples, E. Carter, C.E. Hughes, K.D.M. Harris, J.A. Platts, D.M. Murphy, An ENDOR and DFT analysis of hindered methyl group rotations in frozen solutions of bis(acetylacetonato)-copper(II), *Phys. Chem. Chem. Phys.* 15 (2013) 15214–15222.
  - [42] S.L. Grage, U.H.N. Dürr, S. Afonin, P.K. Mikhailiuk, I.V. Komarov, A.S. Ulrich, Solid state  $^{19}\text{F}$  NMR parameters of fluorine-labeled amino acids. Part II: Aliphatic substituents, *J. Magn. Reson.* 191 (2008) 16–23.
  - [43] M. Imiolek, K. Karunanithy, W.-L. Ng, A.J. Baldwin, V. Gouverneur, B.G. Davis, Selective Radical Trifluoromethylation of Native Residues in Proteins, *J. Am. Chem. Soc.* 140 (2018) 1568–1571.
  - [44] Gast P., Groenen E.J., EPR interactions – g-Anisotropy, *EPR Spectroscopy: Fundamentals and Methods*, in: Goldfarb D., Stoll S. (Eds.), Wiley, 2018, pp. 17–28.
  - [45] M. Bennati, EPR Interactions – Hyperfine Couplings, in: D. Goldfarb, S. Stoll (Eds.), *EPR Spectroscopy: Fundamentals and Methods*, Wiley, 2018, pp. 81–94.
  - [46] Stoll S., Goldfarb D., EPR interactions–Nuclear quadrupole couplings, *EPR Spectroscopy: Fundamentals and Methods*, in: Goldfarb D., Stoll S. (Eds.), Wiley, 2018, pp. 95–114.
  - [47] A. Schweiger, G. Jeschke, Principles of pulse electron paramagnetic resonance, Oxford University Press on Demand, 2001.
  - [48] P.H. Oyala, K.R. Ravichandran, M.A. Funk, P.A. Stucky, T.A. Stich, C.L. Drennan, R.D. Britt, J. Stubbe, Biophysical Characterization of Fluorotyrosine Probes Site-Specifically Incorporated into Enzymes: E. coli Ribonucleotide Reductase As an Example, *J. Am. Chem. Soc.* 138 (2016) 7951–7964.
  - [49] C.J. Jameson, J. Mason, The Chemical Shift, in: J. Mason (Ed.), *Multinuclear NMR*, Springer, US, Boston, MA, 1987, pp. 51–88.
  - [50] C.P. Rosencau, B.J. Jellic, A.D. Gossert, A. Togni, Exposing the Origins of Irreproducibility in Fluorine NMR Spectroscopy, *Angew. Chem. Int. Ed.* 57 (2018) 9528–9533.
  - [51] R.K. Harris, E.D. Becker, S.M.C.d. Menezes, R. Goodfellow, P. Granger, NMR nomenclature. Nuclear spin properties and conventions for chemical shifts (IUPAC Recommendations 2001), *Pure Appl. Chem.*, 73 (2001) 1795–1818.
  - [52] Brownstein S., Bornais J., Universal referencing in multinuclear magnetic resonance spectroscopy, *J. Magn. Reson.* 38 (1980) 131–133.
  - [53] H. Raber, M. Mehring,  $^{19}\text{F}$  Chemical shift tensor in fluorobenzene compounds, *Chem. Phys.* 26 (1977) 123–130.
  - [54] P.D. Ycas, N. Wagner, N.M. Olsen, R. Fu, W.C.K. Pomerantz, 2-Fluorotyrosine is a valuable but understudied amino acid for protein-observed  $^{19}\text{F}$  NMR, *J. Biomol. NMR* 74 (2020) 61–69.
  - [55] P.-P. Zänker, G. Jeschke, D. Goldfarb, Distance measurements between paramagnetic centers and a planar object by matrix Mims electron nuclear double resonance, *J. Chem. Phys.* 122 (2004) 024515.
  - [56] S. Pribitzer, D. Mannikko, S. Stoll, Determining electron–nucleus distances and Fermi contact couplings from ENDOR spectra, *Phys. Chem. Chem. Phys.* 23 (2021) 8326–8335.
  - [57] D.S.G. Henriques, K. Zimmer, S. Klare, A. Meyer, E. Rojo-Wiechel, M. Bauer, R. Sure, S. Grimme, O. Schiemann, R.A. Flowers II, A. Gansäuer, Highly Active Titanocene Catalysts for Epoxide Hydroxylation: Synthesis, Theory, Kinetics, *EPR Spectroscopy*, *Angew. Chem. Int. Ed.* 55 (2016) 7671–7675.
  - [58] E. Salvadori, M. Chiesa, A. Buonerba, A. Grassi, Structure and dynamics of catalytically competent but labile paramagnetic metal-hydrides: the Ti(III)-H in homogeneous olefin polymerization, *Chem. Sci.* 11 (2020) 12436–12445.
  - [59] A. Ashuiev, F. Allouche, N. Wili, K. Searles, D. Klöse, C. Copéret, G. Jeschke, Molecular and supported Ti(III)-alkyls: efficient ethylene polymerization driven by the  $\pi$ -character of metal–carbon bonds and back donation from a singly occupied molecular orbital, *Chem. Sci.* 12 (2021) 780–792.
  - [60] M.I. Arz, M. Straßmann, A. Meyer, G. Schnakenburg, O. Schiemann, A.C. Filippou, One-Electron Oxidation of a Disilicon(0) Compound: An Experimental and Theoretical Study of  $[\text{Si}_2]^+$  Trapped by N-Heterocyclic Carbenes, *Chem. Eur. J.* 21 (2015) 12509–12516.
  - [61] N.J. Stone, Table of nuclear magnetic dipole and electric quadrupole moments, *At. Data Nucl. Data Tables* 90 (2005) 75–176.
  - [62] W. Makulski, K. Jackowski,  $^1\text{H}$ ,  $^{13}\text{C}$  and  $^{29}\text{Si}$  magnetic shielding in gaseous and liquid tetramethylsilane, *J. Magn. Reson.* 313 (2020) 106716.
  - [63] C.J. Jameson, A.K. Jameson, J. Honarbaksh,  $^{19}\text{F}$  nuclear magnetic shielding scale from gas phase studies. II, *J. Chem. Phys.* 81 (1984) 5266–5267.
  - [64] M.R. Baker, C.H. Anderson, N.F. Ramsey, Nuclear Magnetic Antishielding of Nuclei in Molecules. Magnetic Moments of  $\text{F}^{19}$ ,  $\text{N}^{14}$ , and  $\text{N}^{15}$ , *Phys. Rev.*, 133 (1964) A1533.
  - [65] M. Jaszunski, A. Antušek, P. Garbacz, K. Jackowski, W. Makulski, M. Wilczek, The determination of accurate nuclear magnetic dipole moments and direct measurement of NMR shielding constants, *Prog. Nucl. Magn. Reson. Spectrosc.* 67 (2012) 49–63.
  - [66] S. Stoll, A. Schweiger, EasySpin, a comprehensive software package for spectral simulation and analysis in EPR, *J. Magn. Reson.* 178 (2006) 42–55, <https://doi.org/10.1016/j.jmr.2005.08.013>.
  - [67] F. Neese, Software update: the ORCA program system, version 4.0, *Wiley Interdiscip. Rev. Comput. Mol. Sci.* 8 (2018) e1327.
  - [68] A.D. Becke, Density-functional thermochemistry. III. The role of exact exchange, *J. Chem. Phys.* 98 (1993) 5648–5652.

- [69] C. Lee, W. Yang, R.G. Parr, Development of the Colle-Salvetti correlation-energy formula into a functional of the electron density, *Phys. Rev. B* 37 (1988) 785–789.
- [70] S.H. Vosko, L. Wilk, M. Nusair, Accurate spin-dependent electron liquid correlation energies for local spin density calculations: a critical analysis, *Can. J. Phys.* 58 (1980) 1200–1211.
- [71] P.J. Stephens, F.J. Devlin, C.F. Chabalowski, M.J. Frisch, Ab Initio Calculation of Vibrational Absorption and Circular Dichroism Spectra Using Density Functional Force Fields, *J. Phys. Chem.* 98 (1994) 11623–11627.
- [72] F. Weigend, R. Ahlrichs, Balanced basis sets of split valence, triple zeta valence and quadruple zeta valence quality for H to Rn: Design and assessment of accuracy, *Phys. Chem. Chem. Phys.* 7 (2005) 3297–3305.
- [73] S. Grimme, J. Antony, S. Ehrlich, H. Krieg, A consistent and accurate ab initio parametrization of density functional dispersion correction (DFT-D) for the 94 elements H-Pu, *J. Chem. Phys.* 132 (2010) 154104.
- [74] S. Grimme, S. Ehrlich, L. Goerigk, Effect of the damping function in dispersion corrected density functional theory, *J. Comput. Chem.* 32 (2011) 1456–1465.
- [75] C. Adamo, V. Barone, Toward reliable density functional methods without adjustable parameters: The PBE0 model, *J. Chem. Phys.* 110 (1999) 6158–6170.
- [76] M. Ernzerhof, G.E. Scuseria, Assessment of the Perdew–Burke–Ernzerhof exchange–correlation functional, *J. Chem. Phys.* 110 (1999) 5029–5036.
- [77] F. Weigend, Hartree-Fock exchange fitting basis sets for H to Rn †, *J. Comput. Chem.* 29 (2008) 167–175.
- [78] F. Weigend, M. Kattannek, R. Ahlrichs, Approximated electron repulsion integrals: Cholesky decomposition versus resolution of the identity methods, *J. Chem. Phys.* 130 (2009) 164106.
- [79] S. Kossmann, F. Neese, Comparison of two efficient approximate Hartree-Fock approaches, *Chem. Phys. Lett.* 481 (2009) 240–243.
- [80] V. Barone, in: *Recent Advances In Density Functional Methods*, World Scientific, Part I, 1995, p. 287.